Focus Section: Big Data Problems in Seismology

Combined Large-*N* Seismic Arrays and DAS Fiber Optic Cables across the Hengill Geothermal Field, Iceland

Anne Obermann*[1], Pilar Sánchez-Pastor[1], Sin-Mei Wu[1], Christopher Wollin[2], Alan F. Baird[3], Marius Paul Isken[2], John Clinton[1], Bettina P. Goertz-Allmann[3], Torsten Dahm[2,4], Andreas Wuestefeld[3], Peidong Shi[1], Federica Lanza[1], Lea Gyger[1], Selina Wetter[1], Vala Hjörleifsdóttir[5], Nadege Langet[3], Baldur Brynjarsson[5], Philippe Jousset[2], and Stefan Wiemer[1]

Abstract

From June to August 2021, we deployed a dense seismic nodal network across the Hengill geothermal area in southwest Iceland to image and characterize faults and high-temperature zones at high resolution. The nodal network comprised 498 geophone nodes spread across the northern Nesjavellir and southern Hverahlíð geothermal fields and was complemented by an existing permanent and temporary backbone seismic network of a total of 44 short-period and broadband stations. In addition, we recorded distributed acoustic sensing data along two fiber optic telecommunication cables near the Nesjavellir geothermal power plant with commercial interrogators. During the time of deployment, a vibroseis survey took place around the Nesjavellir power plant. Here, we describe the network and the recorded datasets. Furthermore, we show some initial results that indicate a high data quality and highlight the potential of the seismic records for various follow up studies, such as high-resolution event location to delineate faults and body- and surface-wave tomographies to image the subsurface velocity structure in great detail.

Cite this article as Obermann, A., P. Sánchez-Pastor, S.-M. Wu, C. Wollin, A. F. Baird, M. P. Isken, J. Clinton, B. P. Goertz-Allmann, T. Dahm, A. Wuestefeld, *et al.* (2022). Combined Large-*N* Seismic Arrays and DAS Fiber Optic Cables across the Hengill Geothermal Field, Iceland, *Seismol. Res. Lett.* **XX**, 1–17, doi: 10.1785/0220220073.

Introduction

Embarking on exploration and production for any subsurface resource in nonharvested areas is an economic high-risk endeavor, because there is only interpolated knowledge of the subsurface. Precise physical measurements of, for instance, resource abundance, permeability, and temperature are only obtained after the expensive drilling of an exploration well. The hydrocarbon industry has put much effort into reducing this risk by: (1) understanding how their resource is created, (2) imaging relevant geological parameters in the subsurface (layers, faults, seismic velocities and amplitudes, gravity anomalies, etc.), and (3) estimating the probability of a resource discovery. Similar steps are followed in derisking geothermal resource exploration and development. Significant advances have been made by the geothermal industry on how to address all three derisking factors, for different types of environments (Lautze *et al.*, 2017). In particular, in magmatic environments, the physical conditions surrounding the heat source are poorly understood. This deserves attention because magmatic-related geothermal resources are arguably the most utilized type of resource worldwide for power and thermal production. Some of the largest installed geothermal electric capacities can be found, among others, in the USA, Indonesia, Philippines, Turkey, and New Zealand (Rybach, 2014; Craig and Gavin, 2018). Recently, a new frontier for geothermal research has come into focus; the potential use of supercritical fluids as superhot resources (e.g., Reinsch *et al.*, 2017).

For shallow high-temperature systems, substantial experience exists on geoscientific exploration for encountering high-temperature fluids, for example, through geochemical analysis of expelled geothermal fluids, and resistivity imaging of the subsurface. This improved understanding significantly lowers the associated risks. However, it is much more difficult to estimate the fluid recharge of the reservoir and its productivity, which

1. Swiss Seismological Service (SED), ETH Zurich, Zürich, Switzerland, https://orcid.org/0000-0001-6933-6301 (AO); https://orcid.org/0000-0002-1163-5488 (PS-P); https://orcid.org/0000-0001-8330-471X (S-MW); https://orcid.org/0000-0001-8626-2703 (JC); https://orcid.org/0000-0001-5782-245X (PS); https://orcid.org/0000-0002-8168-6766 (FL); https://orcid.org/0000-0002-4919-3283 (SW); 2. GFZ German Research Centre for Geosciences, Potsdam, Germany, https://orcid.org/0000-0002-3992-787X (CW); https://orcid.org/0000-0003-2464-1630 (MPI); https://orcid.org/0000-0001-6432-7422 (TD); 3. NORSAR, Kjeller, Norway, https://orcid.org/0000-0002-1571-6373 (BPG-A); https://orcid.org/0000-0002-3203-7604 (NL); 4. University of Potsdam, Institute of Geosciences, Potsdam, Germany; 5. Reykjavík Energy (OR), Reykjavík, Iceland, https://orcid.org/0000-0003-3275-108X (VH)

*Corresponding author: anne.obermann@sed.ethz.ch

requires mapping out the permeability within the crust. Faults with surface expressions are targeted for drilling, but few tools are available for imaging faults in nonsedimentary settings, especially in volcanically active regions where young volcanic rocks often obscure deeper structural features (Glen *et al.*, 2017). Exploring and producing from deeper and even higher-temperature plays, in which extremely high-energy supercritical fluids can be encountered expose an even higher economic and seismic risk, but potentially present a much higher reward as the power output from an individual well can be significantly higher. In Iceland, a possible tenfold increase in energy output for a single well was suggested utilizing high enthalpy systems (Friðleifsson *et al.*, 2015).

In such volcanic environments, geothermal exploration is just at its start. It is not well understood how fluids and permeability behave near the brittle–ductile transition zone (BDTZ) and close to magmatic heat sources. Therefore, locating drilling targets near these regions poses a challenge. Furthermore, because of the lack of efficient and proven exploration tools for imaging small, deep structures in volcanic environments or the crystalline crust, the geochemical and geophysical signatures of deep high-temperature systems are not well known. Finally, the type of fluids that will be encountered in such high-energy environments has not been established, leaving the demanding material properties of the piping unknown. In the next few years, the third deep well of the Iceland Deep Drilling Project (IDDP-3) is planned at the production field of Reykjavik energy, on the flanks of the Hengill volcano. A successful demonstration of production of super-hot fluid will likely spark an interest in deep, high-energy geothermal production. Up to date, only a few drilling projects were able to simultaneously reach and confirm pressure and temperature of the geothermal fluid present higher than its critical point, that is, the recent IDDP-2 well in Reykjanes, Iceland (Elders *et al.*, 2014), and the Venelle-2 drilling venture in the Larderello geothermal field, Italy (Kruszewski and Wittig, 2018). Other projects found super-hot resources, which were regarded for instance in Los Humeros, Mexico as geothermal wells experiencing ambient temperatures higher than 380°C (Jolie *et al.*, 2020), and in Newberry, South Carolina, as geothermal wells with temperatures higher than 400°C (Cladouhos *et al.*, 2018).

Over the past decades, the Hengill geothermal area has been studied with various geophysical methods, such as resistivity, aeromagnetics, gravity, magnetotellurics, and seismic tomography (e.g., Björnsson *et al.*, 1986; Tryggvason *et al.*, 2002; Árnason *et al.*, 2010; Jousset *et al.*, 2011; Gasperikova *et al.*, 2015; Sánchez-Pastor *et al.*, 2021). Further studies on seismotectonic processes in the region, the automated and real-time generation of earthquake catalogs (Grigoli *et al.*, 2022), the inversions for 3D V_P and V_S velocity models using local earthquakes, and the inversion for a high-resolution 3D V_S model using the ambient seismic field (Sánchez-Pastor *et al.*, 2021) were completed. In particular, the latter study showed interesting local anomalies in seismic velocities in Hverahlið, close to the most powerful boreholes in the region, and in Mosfellsheiði, a so far unexplored region. The co-occurrence of the low-velocity anomalies and the heat sources show the great potential of ambient seismic noise methods as a complementary tool for the exploration of high-enthalpy geothermal fields. Nevertheless, the aforementioned challenges have not been satisfactorily answered, at the scale needed for geothermal exploration. In this context, we set up a dense nodal seismic network and a system of fiber optic cables across the Hengill geothermal area, to tackle these subsurface exploration challenges and image fault structures around the IDDP-3 target region at high resolution. We expect the dense nodal array to allow for high-resolution event localization delineating potential tabular features associated with faults. Body- and surface-wave tomographies using these data will yield better spatial constraints on the velocity anomalies in the top 4 km of the crust. We will gain additional constraints on the subsurface processes from distributed acoustic sensing (DAS), 2D/3D subsurface modeling, and a combination of seismic data with other geophysical measurements, such as magnetic and gravity data.

Here, we present the unique seismic monitoring infrastructure that consists of broadband seismic stations, a dense nodal array, and DAS interrogations along existing telecommunication lines crossing the Hengill geothermal field in the north. We discuss the network layout, characteristics of the recordings, and show initial examples of waveforms that demonstrate the potential of the large datasets.

The Hengill High-Enthalpy Geothermal Area

The Hengill volcano is located at the triple junction of the Reykjanes Peninsula Oblique Rift, the transform-type South Icelandic Seismic Zone, and the West Volcanic Zone, about 30 km east of Reykjavik (Fig. 1d). The region is characterized by eruptive fissures and normal faults (Sæmundsson *et al.*, 2020) forming a N30° striking fissure swarm of around 40 km in length (brown lines, Fig. 1c). This area shows epochs of extensive rifting and subsidence (Sæmundsson, 1992). Dense intrusive rock formations are typically present below 800 m depth and the intrusive boundaries, together with the major faults, make the area highly permeable (Franzson *et al.*, 2005).

The Hengill area is also characterized by elevated heat flow, likely caused by the cooling of magma bodies (e.g., Foulger and Toomey, 1989; Franzson *et al.*, 2010). In this region, the depth of the BDTZ is between 3 and 5 km. The high temperatures and density of faults result in two main high-permeability and high-temperature geothermal systems: Nesjavellir and Hellisheiði. The location of their corresponding power plants is represented with white diamonds in Figure 1. Both plants are run by ON Power producing both electricity and hot water for

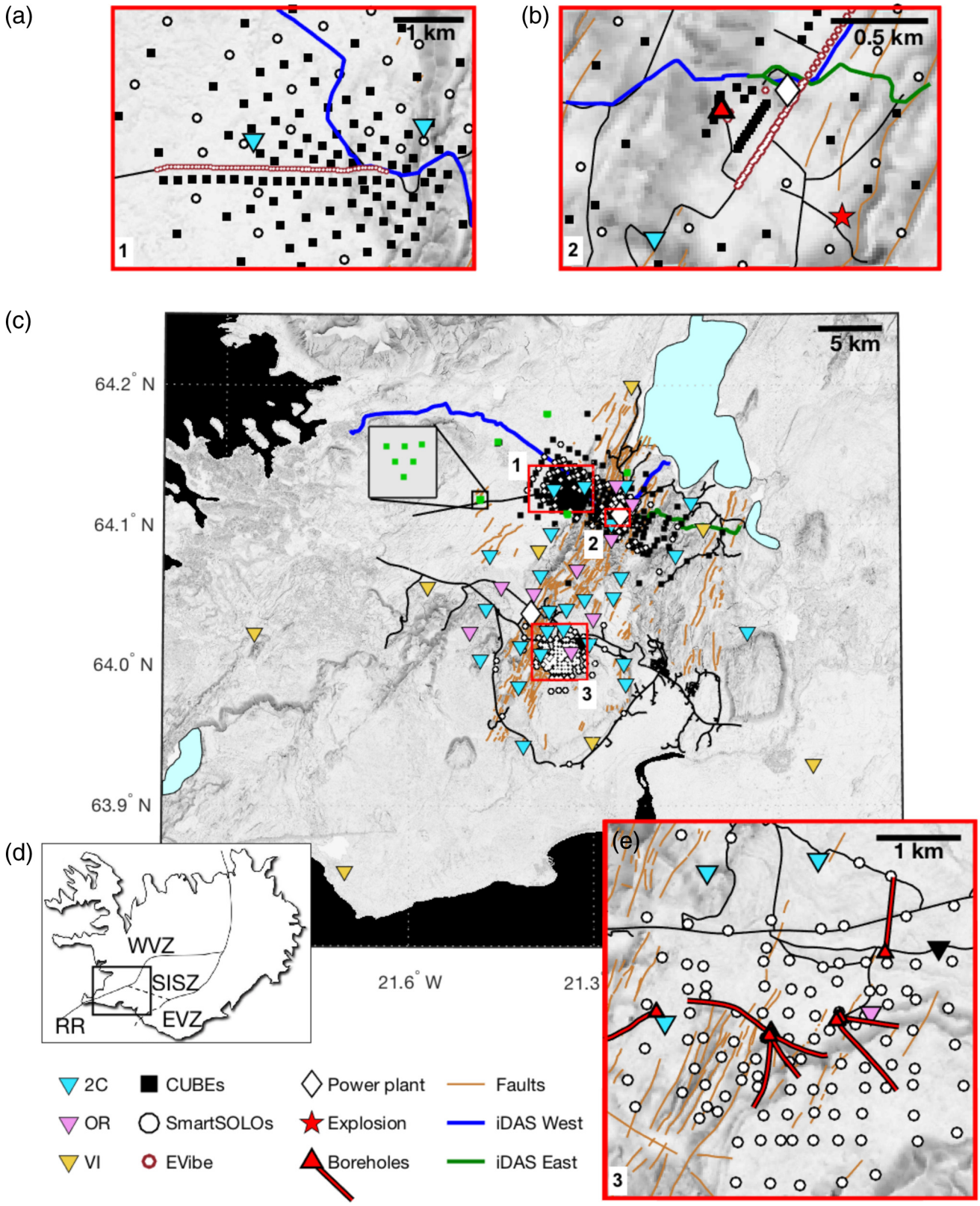

Figure 1. Overview map of the seismic network installations across the Hengill geothermal field. (a,b) Zoom into the location of vibrotruck sweeps along the main road in Mosfellsheiði and around the Nesjavellir power plant, respectively. (c) The permanent (OR, VI) and temporary (2C, YM nodal) seismic networks in Hengill and the location of the telecommunication optical fiber in the north. The red triangle shows the location of the NJ-11 well. (d) The location of the Hengill area at the triple junction. (e) Zoom into the southern nodal array in Hverahlíð and locations of some of the fields most powerful boreholes. The main roads are shown as thin black lines. The color version of this figure is available only in the electronic edition.

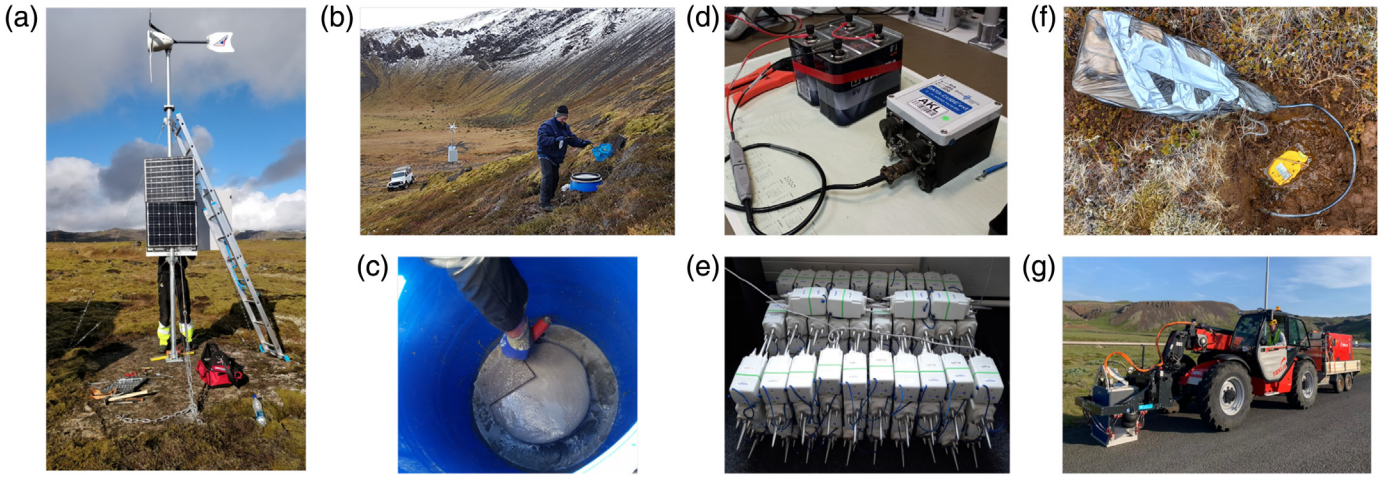

Figure 2. (a–c) Impressions of the field installations for the 2C network and (d–f) the YM arrays. (a) Mast with wind turbine and solar panels for power supply to the sensor and digitizer. (b) Vault with seismic sensor at about 50 m distance from the mast. (c) Concrete socket within vault. (d) Cube with external batteries. (e) Seismic nodes. (f) Field installation of geophone and Datacubes. (g) Vibro-truck used around the Nesjavellir power plant. The color version of this figure is available only in the electronic edition.

district heating and other direct uses. The Nesjavellir power plant (120 MWe, 350 MWth) is located to the northwest of the Hengill volcano and the Hellisheiði power plant (303 MWe, 210 MWth) is located to the southwest. In the coming years, a deep well (>3.5 km) is planned in the Hengill area as a part of the IDDP, with the aim of drilling into the roots of geothermal fields and producing super-hot or even super-critical fluids. For an overview of the geophysical exploration that has been performed over the past decades in Hengill, please refer to Sánchez-Pastor *et al.* (2021).

Seismic Network Design

In the past years, the Hengill geothermal field has received increasing attention as a study site for induced seismicity and related mitigation concepts (e.g. Li *et al.*, 2019; Hjörleifsdóttir *et al.*, 2020; Rossi *et al.*, 2020; Grigoli *et al.*, 2022; Nooshiri *et al.*, 2022).

The backbone seismic network

From November 2018 to August 2021, the Swiss Seismological Service (SED), in partnership with the Iceland Geosurvey (ISOR), the German GeoForschungsZentrum (GFZ), the Dublin Institute for Advanced Studies and Reykjavik Energy (OR), operated 23 seismic stations (10 STS2 120 s, 8 Lennartz 5 s, and 5 Güralp6D 30 s) in the Hengill area (International Federation of Digital Seismograph Networks [FDSN] network code 2C, see Data and Resources, Fig. 1) with the focus to improve and validate advanced technologies for monitoring and controlling induced seismicity (Geothermica project COntrol SEISmicity and Manage Induced earthQuakes [COSEISMIQ]). These stations complemented 10 permanent seismic stations (Lennartz 1 s) from ISOR/On Power (FDSN network codes OR, see Data and Resources), and eight nearby stations that belong to the regional network of the Icelandic Meteorological Office (seven Lennartz 5 s, one Lennartz 1 s, VI network). During the operation period of the 2C network, about 6000 earthquakes with M >0.5 were recorded per year (Grigoli *et al.*, 2022). The 2C and OR stations operated with a sampling rate of 200 samples per second, whereas the VI network recorded at 100 samples per second.

Within the 2C network, each station installation was powered by two solar panels and a wind turbine (Fig. 2a). The wind turbine was installed around 50 m away from the sensor to successfully avoid contaminating the seismic recordings with high-frequency noise. Real-time data transmission was performed using WiFi or 4G cellular network. The rough topography required the setup of additional signal enhancing antennas. The seismic sensors were buried in vaults (around 50 cm deep) with a concrete socket and a thick layer of insulation material to reduce the noise and protect the sensor from temperatures changes (Fig. 2b,c). The depth and insulation proved sufficient. However, there were several challenges related to the harsh weather conditions in the Hengill area that caused data gaps in particular during the winter months (Grigoli *et al.*, 2022). The difficulties to perfectly seal the cable entrance to the vault resulted in several submerged stations, an issue aggravated at sites, which were unfortunately located where standing water gathered during periods of snow melt. Lightning decimated the number of functional Taurus digitizers (Nanometrics) dramatically. The replacement, newer generation Centaur digitizers (Nanometrics), fared better with the weather. Another challenge were strong winds that regularly caused blown fuses at the wind generators. This problem could be improved by removing every second blade.

The 2C network was designed around the main injection and production fields and densified in areas where Reykjavik Energy

considered the drilling of new injection wells, to optimally detect also tiny induced seismic events. With this setup, the COSEISMIQ project goals to control seismicity and manage induced earthquakes should be achieved. Although the abundance of injection and production wells (see Data and Resources) and the simultaneously ongoing operations turned out too challenging for real-time seismic forecasting tools, the network design and the various localized seismic clusters facilitated testing methodological advances of full-waveform based methods for microseismic monitoring operations (Rossi *et al.*, 2020) and neural networks for rapid point-source inversion (Nooshiri *et al.*, 2022).

The nodal seismic network

From June to the beginning of August 2021, we deployed a dense nodal network, consisting of a total of 498 stations. About 207 stations were SmartSolos (IGU16 5 Hz 3C, see Data and Resources) from the University of Geneva and 291 4.5 Hz 3C geophones with DataCubes from the Geophysical Instrument Pool Potsdam (GIPP; Haberland and Ritter, 2016). All stations operated offline with local storage. About 55 DataCubes had a sampling rate of 200 samples per second, whereas the other 245 ran at 400 samples per second. For the SmartSolos, the sampling rate was 500 samples per second. With these settings, the internal battery of the SmartSolos lasted for around 30 days. The DataCubes ran on two external batteries (VARTA, 33Ah, 6V) and lasted for 2.5 months. The temporary installation of all 498 seismic nodes was realized by 12 people within five days. The network was designed to study velocity anomalies and interesting seismic clusters that were observed with the existing backbone network (Sánchez-Pastor *et al.*, 2021). To the north of Hengill, we placed 376 nodes (NJ array) and 119 nodes were located around the Hverahlið geothermal field (HV array, Fig. 1c,e). The NJ array is oriented perpendicular to the fissure swarm and it covers the areas from Mosfellsheiði (Fig. 1c, red square 1) to Hromundartindur in the east crossing the Nesjavellir geothermal field (Fig. 1c, red square 2). With the backbone network, a prominent seismic cluster was detected in Mosfellsheiði lasting from late April to early May 2021 (Duran, 2021). During this time, up to 336 events per day were detected at depths of 3 km, and a maximum magnitude of M_w 3.7 was reached. This seismicity cannot be related to geothermal harvesting operations (injection, production) because there are no deep boreholes in the area. Sánchez-Pastor *et al.* (2021) imaged a slow seismic velocity anomaly coinciding with the location of seismic cluster, although due to the seismic network geometry, this anomaly could not be well constrained. We hence decided to densify the nodal array in this region (Fig. 1a) with the aim to shed light on the origin of the seismic cluster and a potential link to an unknown high-temperature area.

In this NJ array, we also set up six nested triangular mini arrays (green squares in Fig. 1c), in which the interstation distance of the inner triangle is 65 m and the double for outer triangle. These mini arrays are placed surrounding the Mosfellsheiði seismic cluster and the instruments employed are DataCubes recording at 400 Hz. The main purposes of these mini arrays are to enhance the signal-to-noise ratio (SNR) for earthquake location, beamforming of seismic noise (e.g., Roux and Ben-Zion, 2017; Wang *et al.*, 2020) and to experiment with array-derived rotational ground-motion data (Spudich and Fletcher, 2008; Stupazzini *et al.*, 2009; Taylor *et al.*, 2021). The mini arrays will also be used to better constrain a local seismic velocity anomaly observed in Mosfellsheiði in previous studies (Sánchez-Pastor *et al.*, 2021).

Near the Nesjavellir power plant is the well NJ-11 with a depth or 2.2 km (Fig. 1b) that is among the highest temperature wells in the Hengill volcanic complex (380°C at the bottom, Staingrimsson, 1990). For the IDDP drilling, this area is of particular interest, because with such a temperature gradient, it can be expected to find supercritical fluids at relatively shallow depth of less than 3 km, compared with the estimated 5 km elsewhere in the field (Friðleifsson *et al.*, 2003). One explanation for this steep gradient could be a shallow magma pocket (Sánchez-Pastor *et al.*, 2021). With body- and surface-wave imaging, we intend to find an answer to this question. The interstation distance of the nodal array is hence kept dense across Nesjavellir and increases toward the border of the array, covering a total area of 20 km perpendicular and 7 km parallel to the ridge striking. The NJ array is composed of DataCubes and SmartSolos, which were interspaced with the purpose of increasing the resolution during the first month of recordings while also ensuring an optimal array geometry once the SmartSolos ran out of power.

The HV array is located within the Hverahlíð area, where Sánchez-Pastor *et al.* (2021) imaged a low-velocity anomaly that roughly coincides with the location of the most powerful wells. This geothermal field is a subfield of the large Hellisheidi geothermal field. The main purposes of this array are to image this low-velocity anomaly, the origin of which might explain the substantial energy production of the nearby boreholes, with high resolution; and to study the seismicity in this area. The location of the wellhead and trajectories of the boreholes can be observed in Figure 1e. The HV array is exclusively formed by SmartSolo geophones (Figs. 1e, 2e) because one month of data is expected to be sufficient to reach the imaging goal. The extent of the HV array in combination with the COSEISMIQ networks includes ray paths of more than 20 km in several directions, which allows to image the top 4 km of the crust with good resolution.

We also densified the network with nodes in line with the interrogated telecommunication lines and the passage of the vibrotruck (Fig. 1a,b).

The DAS network

In addition to the conventional three-component seismic sensors, we also recorded seismic data along two telecommunication

fiber optic cables with two commercial DAS interrogators. The two cables begin at the center of the survey area near to the Nesjavellir geothermal power plant and run east- and westward, respectively (Fig. 1a–c). Each fiber branch was continuously interrogated from 10 June to 5 August and 17 June to 29 July, respectively.

The western cable has a data gap of seven days from 12 July. Both cables are standard loose-tube single-mode telecommunication fibers and are buried near the surface. The western fiber branch follows paved and dirt roads in a cased conduit over most of its trajectory (Ajo-Franklin *et al.*, 2019). The eastern fiber branch, has a metal-tube protection, is stabilized by metal rods and was directly buried without housing in a plowed trench (Ajo-Franklin *et al.*, 2019). The cables share a 600–meter-long common path segment. The eastern cable has a length of 14 km and was interrogated with a Silixa iDAS (version 2 [v.2]) with 10 m gauge length, 1 kHz sampling rate, and 4 m channel spacing. The western cable is running toward the city of Reykjavik and was interrogated with an ANZA seismic network OptoDAS unit (Waagaard *et al.*, 2021) over a length of 35.8 km, with 10.2 m gauge length, at 2 kHz. The channel spacing was 10 m on the first 5800 m, and 25 m channel spacing thereafter.

The channel spacing of 25, 10, and 4 m for the respective interrogators was chosen as small as possible but was compromised mainly by the data rate and the necessity for autonomous recording for the duration of the campaign. As the OptoDAS unit allows disjoint fiber segments to be interrogated at different spatial sampling periods, a denser spacing was chosen for those near the target area where the occurrence of microseismicity was expected. Thus, wavelengths associated to frequencies below approximately 10, 25, and 70 Hz could be resolved spatially unaliased for a lower bound apparent velocity of 1.2 km/s (Currenti *et al.*, 2021). In total, approximately 30 TB and 24 TB of data were acquired with the OptoDAS and iDAS interrogators, respectively.

Sensor locations along the fiber's previously known trajectory were georeferenced with hammer blows to the surface at approximately 500 m intervals. First arrivals on DAS channels were associated with the respective geolocation. Geolocations of intermediary channels were obtained through linear interpolation along the fiber's trajectory. Loops of slack fiber in previously identified manholes were spared by placing georeferencing hammer blows at each side of the manhole. In between manholes, we thus obtain geolocation uncertainties in the order of the channel spacing.

Data Quality and Availability

Data access

Grigoli *et al.* (2022) document the dataset collected by the backbone network from December 2018 to August 2021. These data are available on European Integrated Data Archive (EIDA; Strollo *et al.*, 2021), using the virtual network COSEISMIQ or directly under the FDSN network codes 2C (SED at ETH Zurich, 2018), 4Q (Dahm *et al.*, 2021), OR (Reykjavík Energy [Iceland], 2016), and VI.

The nodal dataset is collected under the FDSN network code YM (SED at ETH Zurich, 2021) and is curated by the SED. The network information, with full metadata, can be retrieved through EIDA facilities. The data will be made available after the end of the embargo period in January 2025 at this same site.

DAS data will as well be made available at the project end. We aim to make a subset of spatiotemporally decimated time series publicly accessible via known seismological data repositories. However, in particular due to the data volume, a standardized format for the exchange of DAS data is still sought for by the scientific community. In the meanwhile, access and exchange of data can be organized upon request.

Consistent metadata

It is a challenge to produce consistent metadata for the nodal arrays with almost 500 stations. The convention we adopted for recording station coordinates was to take values recorded by the internal Global Positioning System (GPS) receivers of the nodes. Unfortunately, 20% of the stations did not record the elevation properly, of which, 90% were DataCubes. It also became apparent that the precision of the GPS derived elevations was poor. Consequently, we adopted elevations derived from the digital elevation model (DEM) from the National Land Survey of Iceland. For the DataCubes, there is an average offset of around 8 m between the GPS elevations and DEM; for the SmartSolos, this difference is around 6 m. Another challenge is the consistent orientation of the stations in the field. The nodal stations were consistently oriented toward magnetic north. Hence, the station orientations are labeled as Z, 1, and 2, and the azimuth of the horizontal channels includes the 12° of magnetic declination so stations may be rotated to true north. The installation teams used the same smartphone-based compasses and confirmed the orientation while setting up and dismantling the stations. However, stations in the backbone network have been installed and serviced by a variety of different teams and the orientations were a mix of magnetic and geographic (true) north.

To obtain the optimal correction azimuth for the backbone and YM nodal stations, we analyze long-period surface waves from strong teleseismic events. Specifically, we use 20 s period wavefields of both Love and Rayleigh waves from the 29 July 2021 M 8.2 Alaska (USA) event, with an approximate 6250 km great circle distance to the Hengill area. We cross correlate the long-period wavefields centered around the surface-wave arrival (i.e., 1750–2500 s after the origin time) against a reference station, STEKK, where we are confident about the instrument installation and orientation toward true north. We rotate the horizontal channels with a one-degree interval to find the

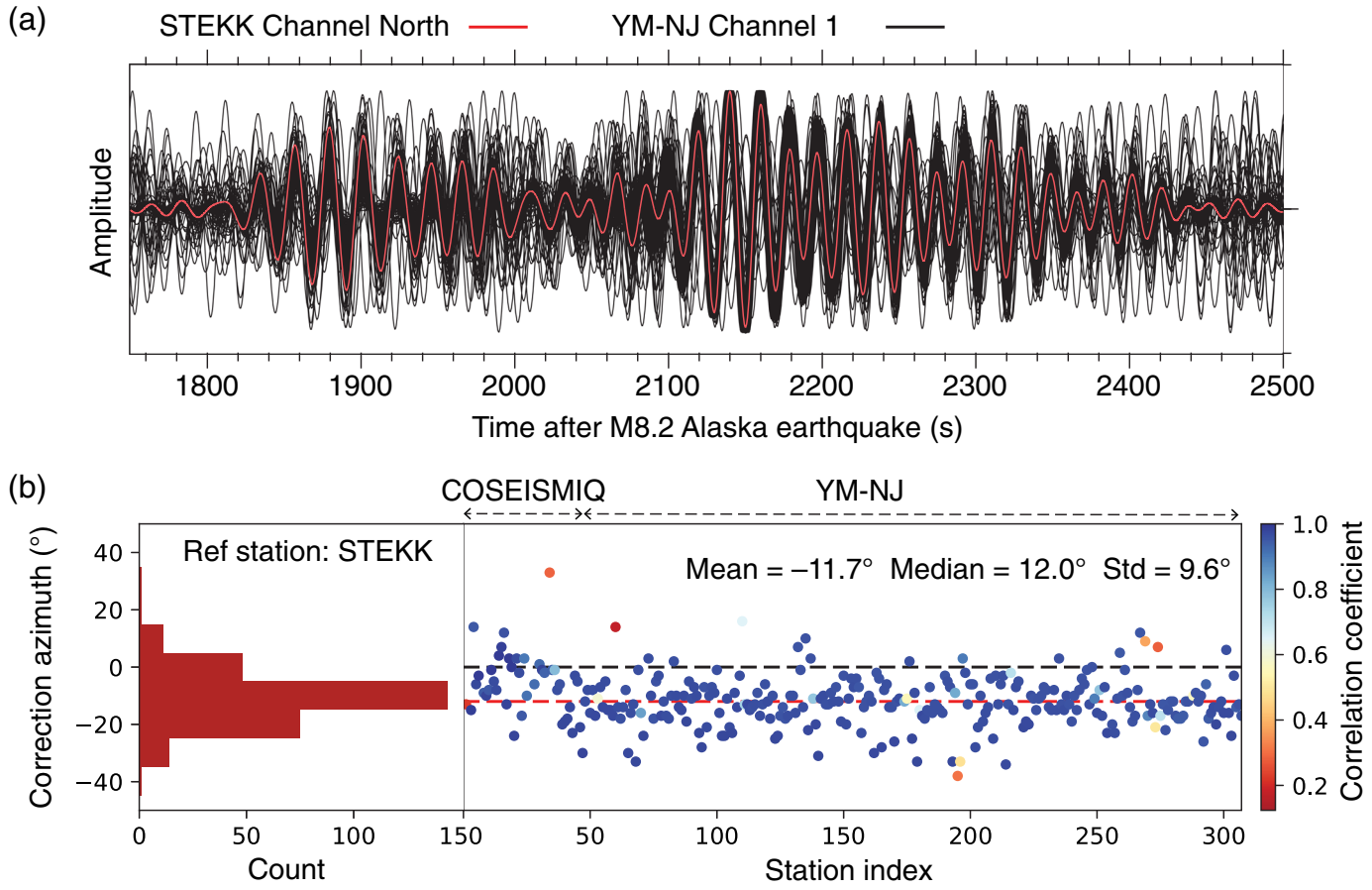

optimal correction azimuth, which is determined when the paired waveforms reach the highest correlation coefficient.

We found that the nodal stations have a consistent mean of 12° difference with regard to the magnetic declination but also around a 10° standard deviation, likely related to the challenges in deployment and uncertainty of measurement in the field (Fig. 3). The optimal correction azimuths from the backbone permanent network exhibit a larger discrepancy.

The resulting correction azimuth is integrated into the metadata. However, given the limitations of viable earthquakes during the time of deployment, the method could only be performed on the part of the network that was operating during the passage of the earthquake, and the reported azimuth reflects the status of the instrument at this, which is at the near end of the 2C network operation, and after the closure of the YM-HV array.

Data completeness and quality

From the 498 YM nodal stations that were deployed, we could retrieve data from 495 stations. Two SmartSolos were unreadable and one station remained lost in the field. In addition, three DataCubes have only very short recordings. The remaining nodes recorded have complete recordings for one, or two months, respectively (Fig. 4).

In Figure 5, we display the median power spectral densities (PSDs) for each of the three components of the YM nodal stations for the full experiment duration. We observe a similar instrument performance, especially below 1 Hz and at the 7 s microseism. About 50 Hz noise is observed at some sites and the anti-aliasing filter effects are visible. The PSDs show the very large variety in the noise conditions between 2 and 50 Hz—up to three orders of magnitude—that reflect very different site conditions.

In addition, we present week-long spectrograms from three representative nodal sites; at a remote site (Fig. 6a), in vicinity of a larger road (Fig. 6b) and close to a power plant with substantial steam production (Fig. 6c). We record the 7 s microseism at all sites, amplified in periods of turbulent weather. The M 8.2 Alaska earthquake on 29 July 2021 is clearly visible at lower frequencies. At high frequencies (>8 Hz), the pipes around the power plant dominate the recordings for close-by stations (Fig. 6c).

Figure 3. (a) Long-period surface waves from the 29 July 2021 M 8.2 Alaska earthquake recorded at the reference station STEKK (red) and the YM nodals (black). The dominant period is 20 s. (b) Optimal correction azimuth (dots) for each of the available backbone (2C, ON, VI) and YM-NJ stations based on the reference station STEKK. The maximum correlation coefficient is color coded. Statistical values are denoted at the upper-right corner, and the distribution is shown on the left-hand-side histogram. The black- and red-dashed lines indicate the orientation to true north and magnetic north, respectively. COSEISMIQ, COntrol SEISmicity and Manage Induced earthQuakes The color version of this figure is available only in the electronic edition.

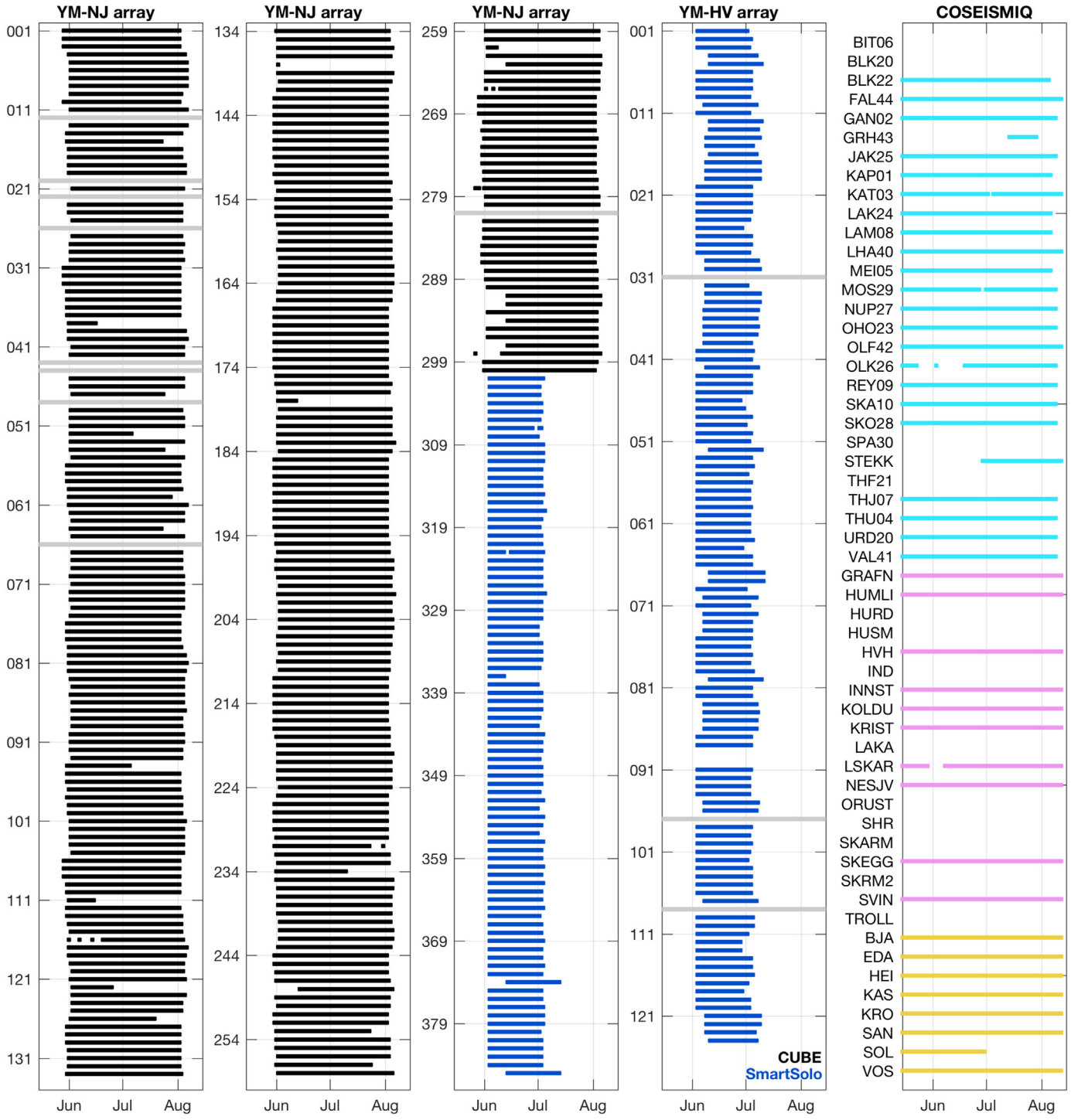

Initial Observations

In this section, we show some initial observations that highlight the potential of the dataset for various follow up studies.

Vibroseis experiment

We had the opportunity to acquire an additional, high-frequency dataset from an electrical seismic vibrator truck (Fig. 2g) around the Nesjavellir power plant.

The vibroseis experiment was conducted in the form of two surveys between 19 and 23 July 2021. The first survey (Fig. 1b)

Figure 4. Data completeness for the YM nodal and COSEISMIQ networks. The data recordings from the DataCubes are shown in black and from the SmartSolos in blue. Not existing stations are shown with a light gray bar. The name of the array together with the sensor numbers on the left side of the columns form the station names for the nodal array. The colors for the COSEISMIQ network indicate the different subnetworks involved. The color version of this figure is available only in the electronic edition.

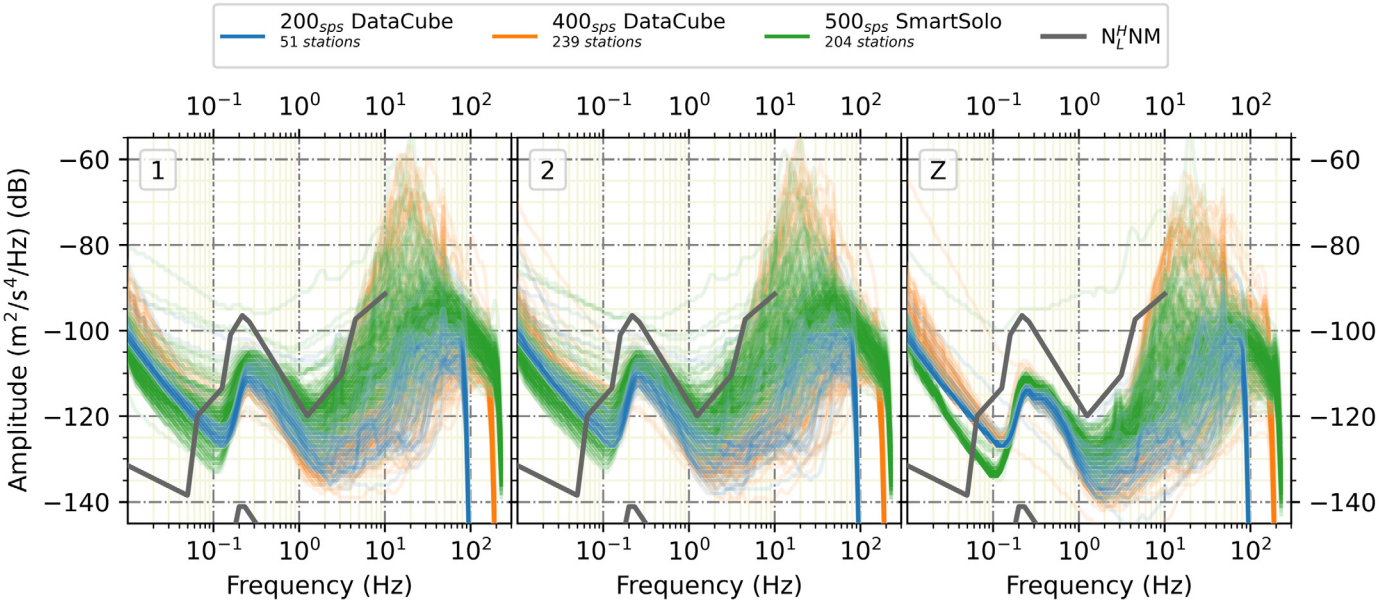

Figure 5. Mean power spectral density for each seismic nodal station. Different color codes are used for 200 Hz DataCubes (blue), 400 Hz DataCubes (orange), and 500 Hz SmartSolos (green). Shown are from left to right the two horizontal components 1 and 2 and the vertical component. The U.S. Geological Survey (USGS) low- and high-noise models (Peterson, 1993) are indicated with the black lines. The color version of this figure is available only in the electronic edition.

took place next to the Nesjavellir power plant with three shooting points close to the borehole NJ-11 (very high temperature well) and 75 shooting points along a 2 km profile on the road leading to the power plant. Several DataCubes sampling at 400 Hz were allocated to the survey with an interstation distance varying along the profile. Close to the borehole, the geophones were evenly spaced with an interstation distance of 20 m. The main goal of this survey is to image the subsurface around the NJ-11 borehole and obtain indications of potential magma pockets.

The second survey took place along a road in the western part of the Nesjavellir area, in Mosfellsheiði (Fig. 1a), where a seismic cluster and low-velocity anomaly had been detected (Sánchez-Pastor *et al.*, 2021). The profile was approximately 3 km long and comprised 65 shooting points. About 17 DataCubes (400 Hz) were allocated to this survey with an interstation distance of 200 m at 150 m from the road. The main purpose of this survey is to image with high-resolution velocity and attenuation structure at shallow depths of this unexplored area.

The vibrotruck used for this experiment (see Data and Resources) had a force of 10 kN. Each shooting point comprised seven sweeps with a duration of 15 s. The frequency of the sweeps started a 2 Hz and was linearly increased up to 100 Hz. A taper of 550 ms was applied at the beginning and end of each sweep. Some tests were made on the first day of the experiment using four DataCubes to define the best configuration of the sweeps and ensure there was no timing issue.

First data processing results show a challenging dataset due to various reasons. First, active source experiments in magmatic environments are generally more difficult to handle due to the high scattering and attenuation. This entails a low SNR and truck sweeps can be hardly observed at more than 1 km distance (Fig. 7c). The high local seismicity complicates the identification of the truck signal in the seismic records. Some of these issues could have been addressed by increasing the number of geophones along the road, the power of the truck, and the number of sweeps per point.

Toward a seismic event catalog

For the backbone COSEISMIQ network, Grigoli *et al.* (2022) produced a set of automated absolute and relative seismic catalogues using the SeisComP3 software (Hanka *et al.*, 2010). For the dense YM array, using standard tools such as SeisComP3, it is challenging to build a similar seismic catalog that can make optimal use of very short interstation spacing that provides precise earthquake locations with a far lower completeness magnitude. Reasons include very short interevent times that require optimization of pickers as well as pick and origin associators. Event magnitude estimates also need to be adopted to account for the very small events. Instead, we process the collected continuous seismic data with an automatic event detection and location workflow (MAchine Learning aided earthquake MIgration location [MALMI], Shi *et al.*, 2022) to obtain a seismic catalog. In this workflow, a pretrained machine learning (ML) model (EQTransformer, Mousavi *et al.*, 2020) is first used to efficiently process the seismic data and predict the continuous *P*- and *S*-phase probabilities. Without the need for phase picking and

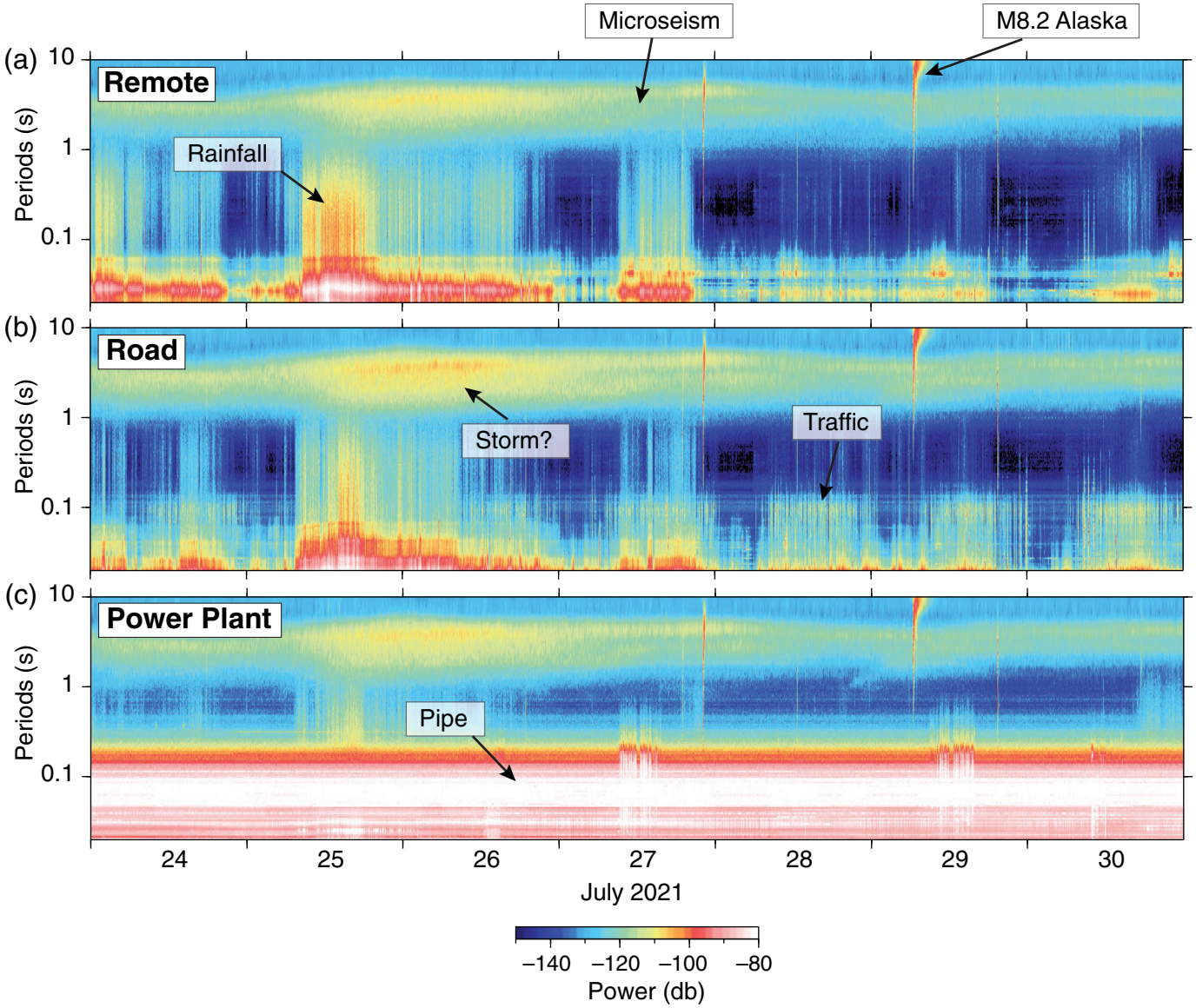

Figure 6. Spectrograms of seismic nodal data from 24 to 30 July 2021 recorded (a) at a remote site (NJ107), (b) by a major road (NJ172), and (c) by the Nesjavellir power plant (NJ160). The color version of this figure is available only in the electronic edition.

association, seismic events are then detected based on the predicted phase probabilities of the array with their time range propagating across the array being simultaneously determined (Fig. 8a). We use all available stations, including the backbone seismic stations (2C, OR, and VI) and the nodal stations (NJ and HV arrays), to detect and locate seismic events occurring in the Hengill region. To also detect microseismic events, which might be only detectable at a few stations close to the source, a fairly low detection threshold is adopted, that is, eight stations with a *P*- or *S*-phase probabilities larger than 0.05. Following the event detection step, backprojection is subsequently used to stack the phase probabilities of the detected events, remove false detections, and obtain event location and origin time (Fig. 8b–d). Combining ML and waveform migration techniques allows us to efficiently produce a reliable automatic catalog while lowering the magnitude of completeness of the catalog. This catalog will constitute the baseline for further seismological analysis.

Different types of seismic signals

In Figure 7, we show different event classes that can be observed on the YM nodal data. In Figure 7a, we show a typical local seismic event with a magnitude of M_w 2.4 that occurred on 23 July 2021. Such an event can be observed over the entire array and has over 260 detections of clear *P* and *S* phassaases (the HV array was already dismantled). During the time of deployment, a Meteoroid was recorded passing by the nearby Thingvellir national park on 2 July 2021 (Fig. 7b). The presence of the dense array offers the unique opportunity to test different Meteoroid source models and theoretical directivity effects.

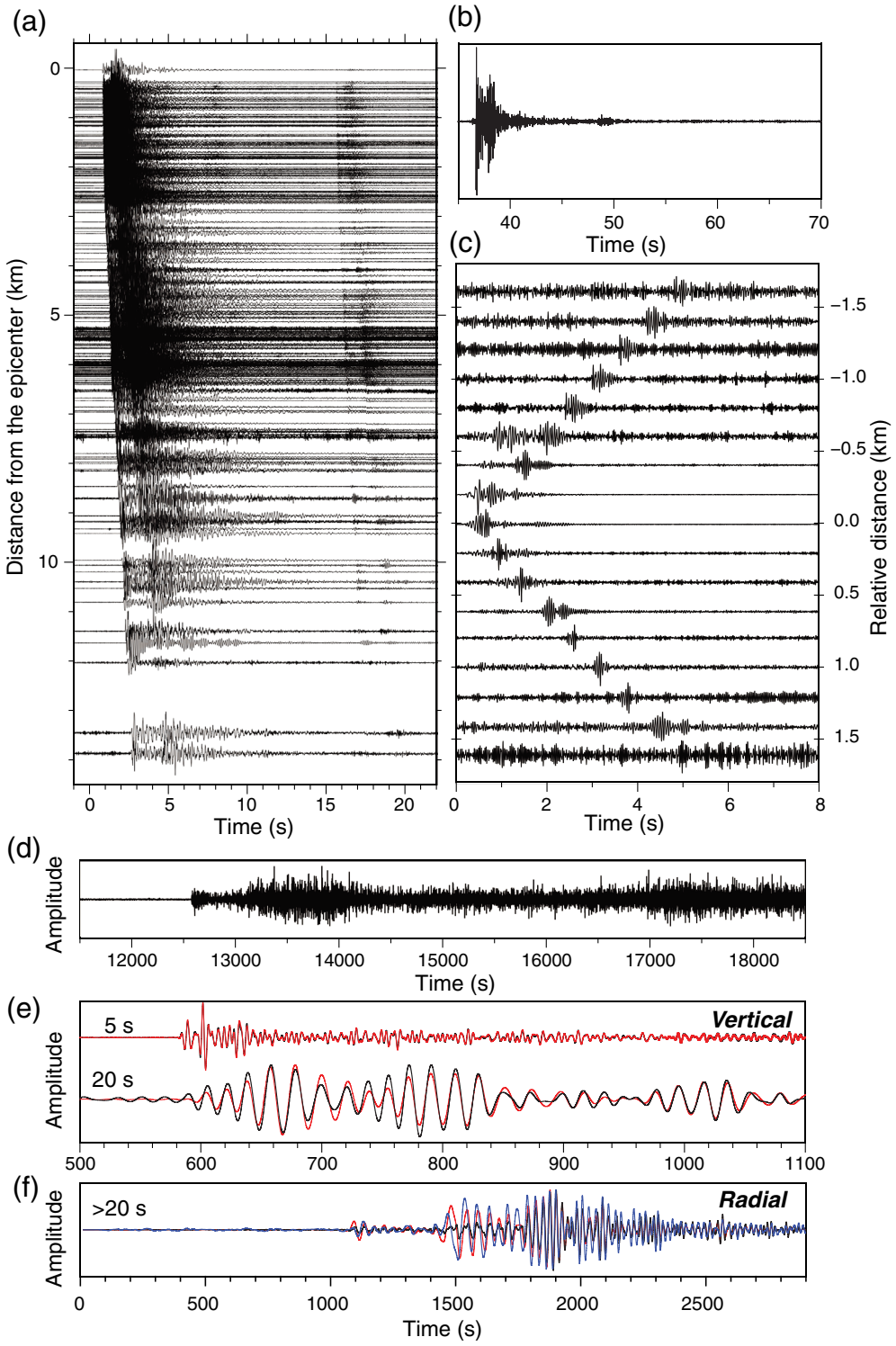

Figure 7. Different event classes observed on nodal data: (a) exemplary local seismic event with M_w 2.4, (b) acoustic signal of a Meteoroid in the adjacent Thingvellir national park, (c) exemplary vibrotruck sweep, (d) well explosion close to the Nesjavellir power plant (see Fig. 7d), (e) 2021 M 8.2 Alaska earthquake as observed on the vertical component of a nodal (black, NJ027) and adjacent broadband station (red, OLF42), and (f) 2021 M 8.2 Alaska earthquake as observed on the radial component of the nodal (black), broadband (red), and distributed acoustic sensing (DAS) (blue). The color version of this figure is available only in the electronic edition.

In Figure 7c, we show a typical Vibro-truck sweep close to the Nesjavellir power plant. These data are expected to shed light on the source of the powerful wells in the region. On 14 June 2021, a well in vicinity of the Nesjavellir power plant exploded (Fig. 7d). With help of the dense array and coda-wave interferometry, we want to investigate whether there were observable indications for the well instability. Very interesting is also the recording of the 28 July 2021 M 8.2 Alaska earthquake on the seismic arrays (Fig. 7e,f). The comparison of a nodal and adjacent broadband station shows the capacity of the nodes to accurately record low-frequency signals (20 s) (Fig. 7e). In addition, the DAS recordings match very well with the radial component of the seismic stations, especially in the lower frequency range (Fig. 7f). For this comparison, we used the horizontal components of the seismic stations, corrected their azimuth for orientation, and rotated them to the radial component of the DAS cable. The nodal data have a quite good performance except for the >50 s energy 1500 s arrival time.

Figure 9 shows the DAS recordings of both fibers of the previously discussed local M_w 2.4 event (Fig. 7a). Clear *P*- and *S*-wave onsets can be observed throughout the trajectories of both fibers. A substantially elevated noise floor can be observed where the fibers pass near Nesjavellir power plant, that is, near the location of the DAS unit interrogating the eastern fiber (Fig. 9a, green triangle). The elevated noise floor at the beginning and end of the eastern fiber is likely due to the

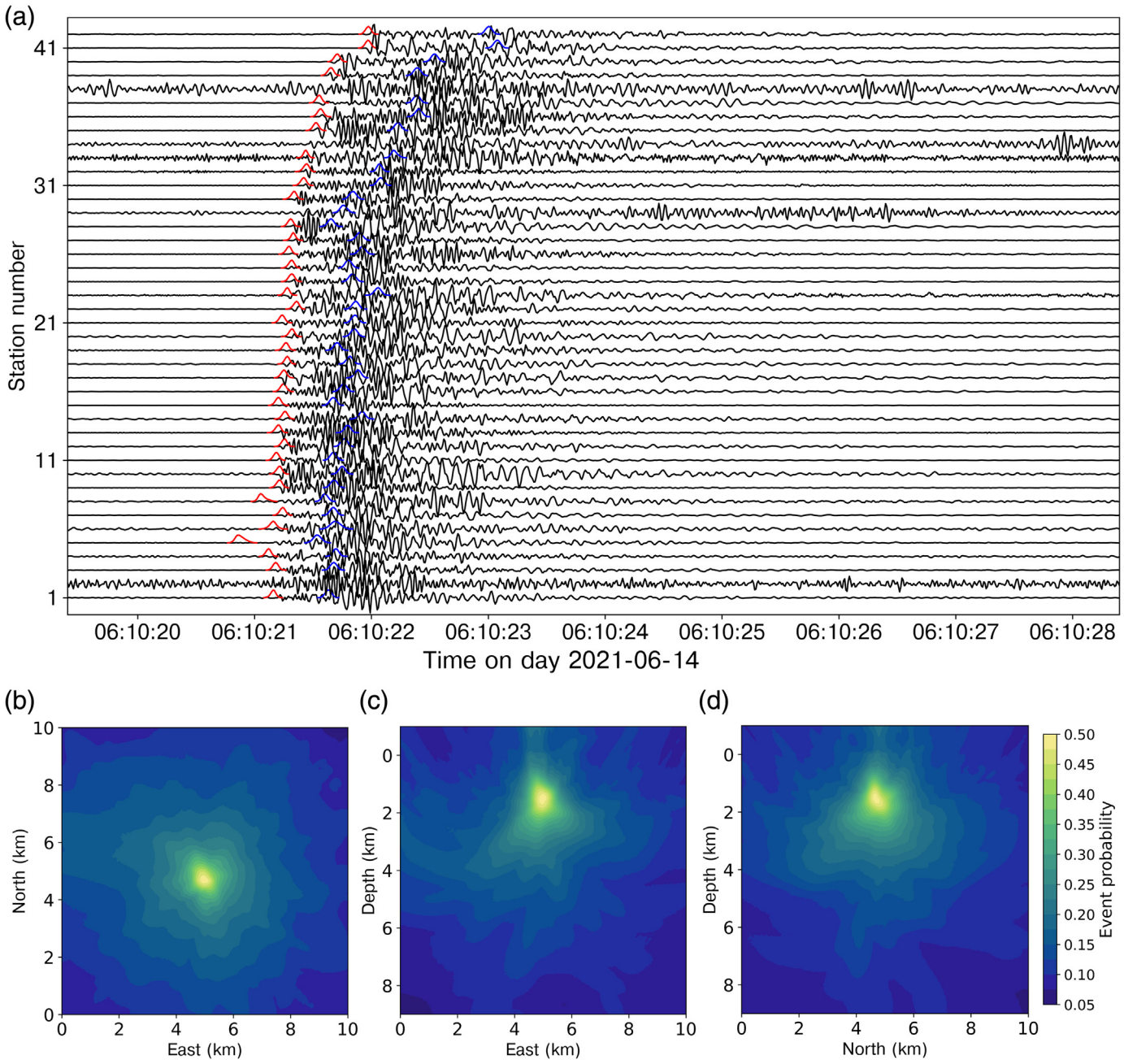

Figure 8. A microseismic event that has been detected and located by the MAchine Learning aided earthquake MIgration location (MALMI) workflow. (a) Normalized vertical-component waveforms (2–50 Hz) at part of the YM nodal stations with the machine learning predicted *P*- (red line) and *S*-phase (blue line) probabilities overlaid upon the waveforms. Migration profiles corresponding to this event are shown in (b) the northeast profile, (c) the east-depth profile, and (d) the north-depth profile, respectively. The color version of this figure is available only in the electronic edition.

urban agglomerations crossed in these areas. Besides the body-wave onsets, a significant variation of the amplitudes of neighboring fiber segments can be observed throughout both trajectories too. Several reasons could be responsible for this. Most obviously, the coupling of the fibers with the ground may differ depending on the peculiarities of the installation of a fiber stretch (Ajo-Franklin *et al.*, 2019; Currenti *et al.*, 2021). Further, the strain response depends on the slowness of the incoming wavefront and thus also on the fiber's orientation (Jousset *et al.*, 2018; Lindsey *et al.*, 2020). However, the systematically elevated amplitude levels in the Mosfellsheiði area (Fig. 1a) approximately between 7 and 10 km of the western fiber may also be caused by the here observed low-velocity anomaly (Sánchez-Pastor *et al.*, 2021). Some fiber segments respond to the earthquake with reverberations seen as long tailed coda waves, for instance at 11 km of the eastern fiber. This may indicate local site effects or the fibers' crossing of fault zones where low-velocity layers trap the seismic energy (Hillers

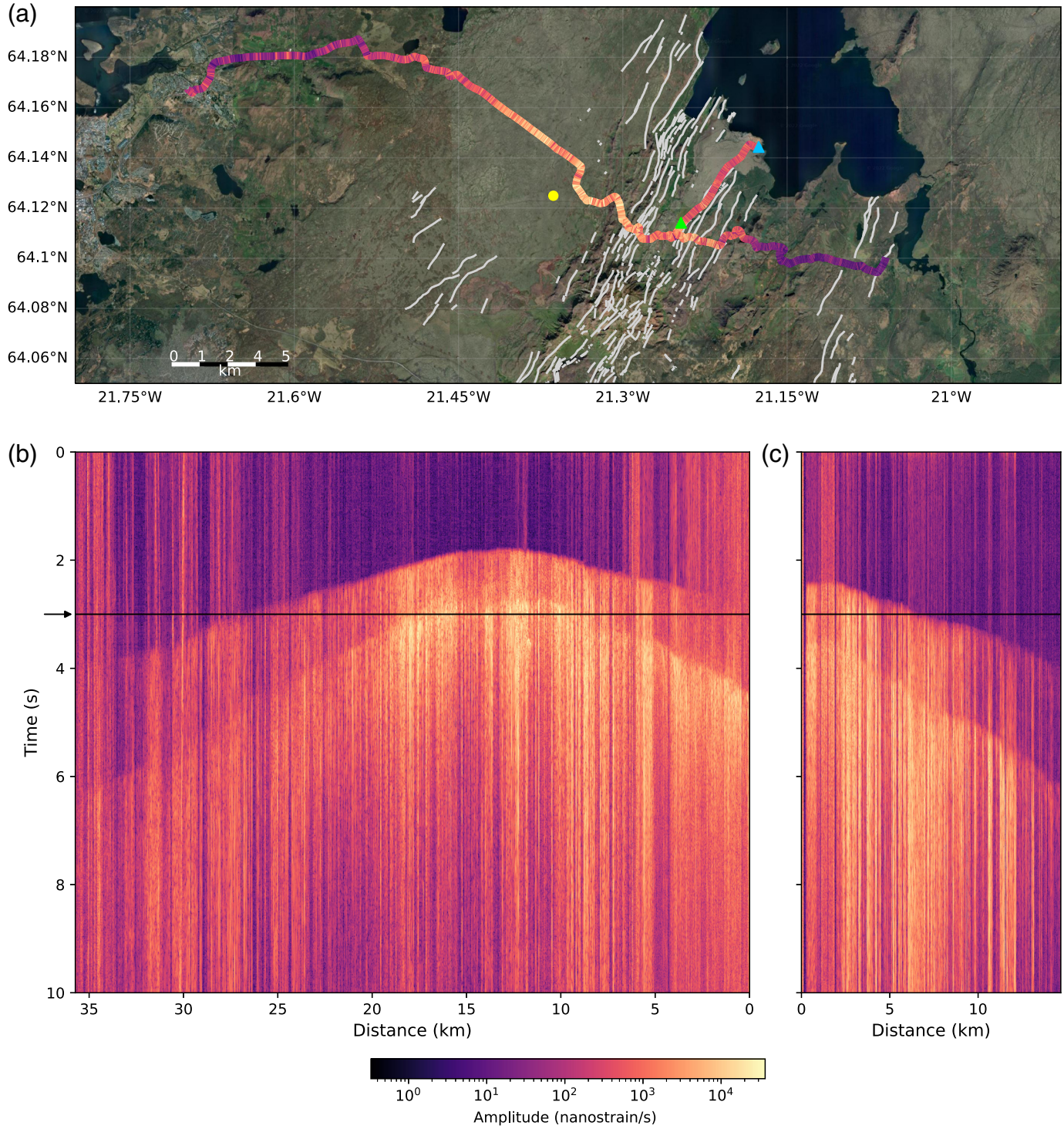

Figure 9. Local earthquake (M_w 2.4) recorded on the western and eastern fiber optic cables. (a) Map showing the event location (yellow dot) and the cable geometry with a time snapshot of the recorded signal overlaid. Mapped faults are shown as gray lines. Blue and green triangles indicate the locations of the OptoDAS (western) and iDAS (eastern) interrogators, respectively. Panels (b) and (c) show waterfall plots for both cables, respectively. The amplitudes are given as the envelope of the 1–40 Hz band-pass filtered strain-rate signal plotted with a logarithmic color scale. The black horizontal lines marked by an arrow indicate the time snapshot of the data overlaid on the cable map. The color version of this figure is available only in the electronic edition.

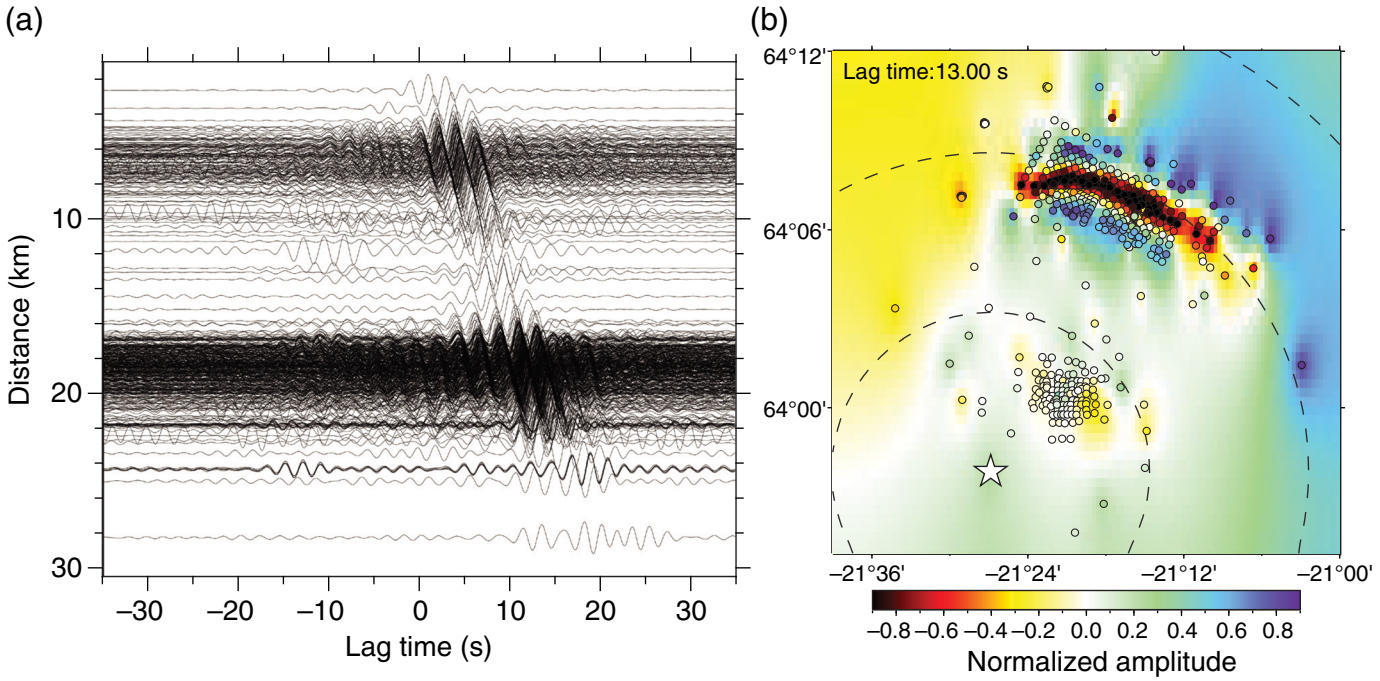

Figure 10. Cross-correlation functions of (a) 2 s waveform and (b) its mapped amplitude at 13 s lag time across the study area. The exact value is plotted at each of the stations (open circles) and the background is interpolated. The source station (HV121) is marked with a white star. The dashed contours represent the distance to the source station with an interval of 10 km. The amplitude is color coded showing a clear wavefront propagating through the northern YM-NJ array. The color version of this figure is available only in the electronic edition.

et al., 2014; Jousset *et al.*, 2018). However, the cause of this observation is still subject of investigation.

Noise cross correlations

To perform noise-based body- and surface-wave tomographies, the quality of the cross correlations is very important. In Figure 10a, we show the example of a cross-correlation function computed from data between June and July 2021 recorded by the virtual source station at HV-121 (white star, Fig. 10b) and the receiver stations (open circles, Fig. 10b) across the network. The following processing is applied: The continuous recording at each station is prefiltered (Butterworth low-pass filter at 10 Hz), decimated to 20 samples per second, deconvolved from the instrument response, and split into 20 min segments. For each of the time segments, we cross correlate the vertical component between station pairs (i.e., ZZ) across the array after spectral whitening. To avoid spurious signals, potentially from earthquakes and traffic, we exclude 20% of the time segments that have larger maximum amplitude for the process. Finally, we normalize each cross correlation based on its maximum amplitude and linearly stack all time segments.

The surface waves in the ambient noise correlations exhibit good signal quality (Fig. 10a). Using a virtual source station near the southern end of the network, the cross correlations show coherent Rayleigh waves moveout across the study area and demonstrate a strongly asymmetrical pattern (Fig. 10a). A clear low-velocity anomaly near Mosfellsheiði can be seen from the delayed Rayleigh-wave arrivals (Fig. 10b), consistent with the previously observed low shear-wave velocity structure using the sparse backbone network (Sánchez-Pastor *et al.*, 2021). An explanation for the low velocity is that the surface geology in most of this area is covered by interlacing layers of hyaloclastites and fresh lavas with an abundance of open pores. The asymmetry indicates the presence of a dominant noise source environment from the microseisms south of Iceland. We selected the cross-correlation function of two stations belonging to the NJ and HV arrays, separated by 27.9 km (Fig. 11a) and computed the group velocities of the Rayleigh waves (Fig. 11b). The dispersion curve was computed following Schimmel *et al.* (2017) and exhibits frequency range of 1–5 s with sufficient energy for a clear dispersion curve extraction and hence imaging applications. This frequency range and the quality of the dispersion curve are largely consistent with the observations from the backbone network using 1.5 yr of data (Sánchez-Pastor *et al.*, 2021).

Conclusion and Outlook

We present the seismic networks (backbone, YM nodal, and fiber optic systems) that were operating across the Hengill geothermal field in summer 2021. Around 498 seismic stations were temporarily set up on top of regions of particular interest around the Nesjavellir geothermal field in the north that showed swarm activity and low-seismic velocity anomalies in previous studies, and on top of the Hveralid geothermal

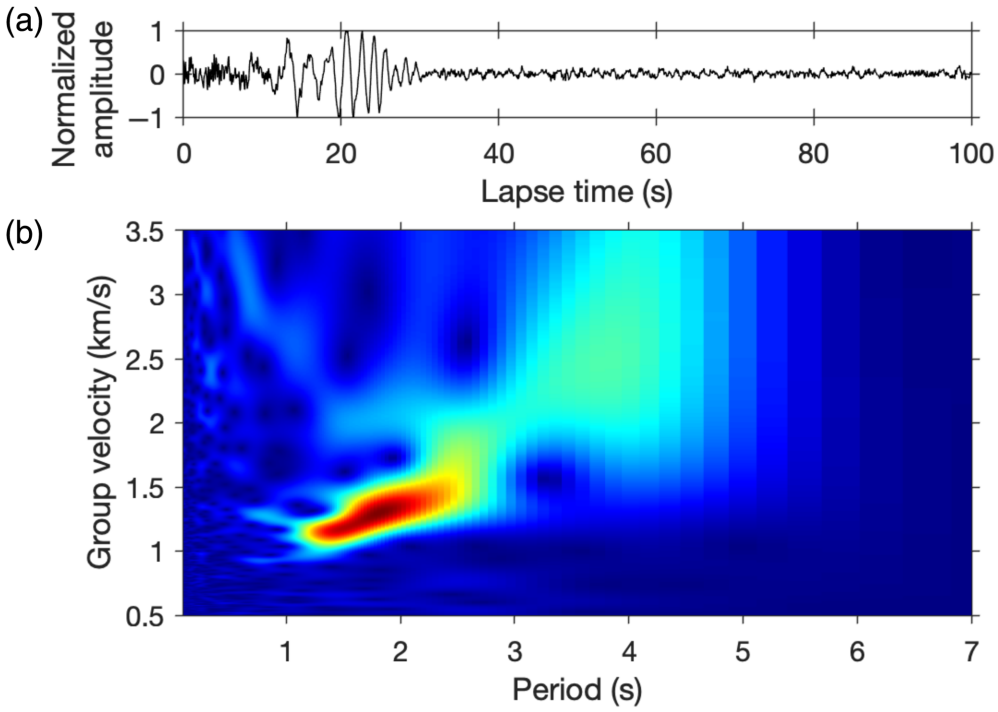

Figure 11. (a) Causal part of the cross correlation of HV121 and NJ010. The stations are separated by 28 km. (b) Wavespeed period representation of (a). The color version of this figure is available only in the electronic edition.

subfield in the south, where some of the most powerful production wells are located. This is by far the largest seismic network, by number of seismometers, installed in Iceland to date. The good SNR of the data presented here is exemplary of the high quality of the collected dataset. The ongoing research is twofold. We will apply classical microseismic techniques (e.g., event detection and location) and enhance and apply innovative methods for imaging in complex basaltic and granitic environments with few or no strong reflectors. This includes tomographic methods such as noise-based interferometry and attenuation tomography.

These methodological improvements will enable us to detect and map structures (i.e., damage zones with enhanced permeability, high-temperature areas) with unprecedented resolution. In addition, *b*-value imaging will provide further insights into the fault structures. We will also estimate source parameters such as stress drop and compare these to inverted parameters, such as Poisson's ratio and Q. The systematic variation of these combined parameters will provide insight into fluid migration patterns within the reservoir and may be indicative of supercritical fluids, which could be of significant economic value in these magmatic geothermal plays. Modeling will be used to analyze the effect of different overburden structures on the image quality of the target area, for example, different basalt layers changing in shape and size. The use of the datasets in these more detailed studies will increase the scientific impact, shedding light at the detection, and imaging of fault zones and areas hosting potentially supercritical fluids at unprecedented resolution.

Data and Resources

The nodal dataset is collected under the International Federation of Digital Seismograph Networks (FDSN) network code YM (Swiss Seismological Service [SED] at ETH Zurich, 2021) and is curated by the SED. The network information, with full metadata, is discoverable on European Integrated Data Archive (EIDA; http://eida-federator.ethz.ch/fdsnws/station/1/query?net=YM&format=text&level=station&nodata=404). The data are currently restricted and will be made available after the project end in January 2025 at this same site. Distributed acoustic sensing (DAS) data will as well be made available at the project end. We aim to make a subset of spatiotemporally decimated time series publicly accessible via known seismological data repositories. However, in particular due to the data volume, a standardized format for the exchange of DAS data is still sought for by the scientific community. In the meanwhile, access and exchange of raw data can be organized upon request. The information about COntrol SEISmicity and Manage Induced earthQuakes (COSEISMIQ 2C) is available at 10.12686/sed/networks/2c. The information about OR - Reykjavik Energy is available at 10.7914/SN/OR. The Orkustofnun's map viewer is available at https://map.is/os/#. The information about SmartSolo is available at https://smartsolo.com. The information about Seismic Mechatronics is available at https://seismic-mechatronics.com/. All websites were last accessed in June 2022.

Declaration of Competing Interests

The authors acknowledge that there are no conflicts of interest recorded.

Acknowledgments

The authors like to thank the field crew that endured the dreadful weather conditions in Hengill during the installation and dismantling of the 500 nodes! The authors thank Gregor Hillers and Thomas Planès for their insightful comments on the successful setup of nodal arrays. The authors thank the Mila telecom company and in particular Halldór Guðmundsso and Adolf Þór Lúðvíksson for providing their dark telecommunication fiber along with its technical and geographic parameters and their onsite support. The authors also thank Martin Lipus and Lioba Virchow (German GeoForschungsZentrum [GFZ])

as well as Hanna Blanck (Vedur, Iceland) for conducting the georeferencing campaign for the eastern fiber. About 291 5 Hz 3C geophones and datacubes were provided by the Geophysical Instrument Pool Potsdam (GIPP) of GFZ, Grant Number GIPP202111. About 207 SmartSolos were provided by the University of Geneva. The presented work has been accomplished within the framework of the Geothermica project Derisking exploration for geothermal plays in magmatic environments (DEEPEN; Grant Number 03EE4018). M. I., C. W., and S.-M. W. have been directly supported by this project. B. G. A., A. B., A. W., and N. L. are supported by the Norwegian Research Council ENERGIX program (Grant Number 317676). P. S. and F. L. are supported by the Geothermica project Innovation for De-Risking Enhanced Geothermal Energy Projects (DEEP; Grant Number 731117). P. S.-P. received funding from the European Research Council (ERC) under the European Union's Horizon 2020 research and innovation program Real-Time Earthquake Risk Reduction for a Resilient Europe (RISE; Grant Number 821115) and from the Swiss National Science Foundation (Grant Number 200021-18196). The authors thank Roman Racine, Stefan Heimers, and Frederic Massin for support in integrating and curating the waveforms and metadata for the YM network, as well as preparing the power spectral densities (PSDs). The authors thank Gregor Hillers for the very detailed and constructive review that helped improve the article.

References

Ajo-Franklin, J. B., S. Dou, N. J. Lindsey, I. Monga, C. Tracy, M. Robertson, V. R. Tribaldos, C. Ulrich, B. Freifeld, T. Daley, *et al.* (2019). Distributed acoustic sensing using dark fiber for near-surface characterization and broadband seismic event detection, *Sci. Rep.* **9,** no. 1, doi: 10.1038/s41598-018-36675-8.

Árnason, K., H. Eysteinsson, and G. P. Hersir (2010). Joint 1D inversion of TEM and MT data and 3D inversion of MT data in the Hengill area, SW Iceland, *Geothermics* **39,** no. 1, 13–34.

Björnsson, A., G. Hersir, and G. Björnsson (1986). The Hengill high temperature area, SW Iceland: Regional geophysical survey, *Geothertm. Resour. Counc. Trans.* **10,** 205–210.

Cladouhos, T. T., S. Petty, A. Bonneville, A. Schultz, and C. F. Sorlie (2018). Super hot EGS and the Newberry deep drilling project, *43rd Workshop on Geothermal Reservoir Engineering*, Stanford University, Stanford, California, 1–13.

Craig, W., and K. Gavin (2018). *ICE Themes Geothermal Energy, Heat Exchange Systems and Energy Piles*, ICE Publishing, London, United Kingdom.

Currenti, G., P. Jousset, R. Napoli, C. Krawczyk, and M. Weber (2021). On the comparison of strain measurements from fibre optics with a dense seismometer array at Etna volcano (Italy), *Solid Earth* **12,** no. 4, 993–1003.

Dahm, T., S. Cesca, S. Heimann, S. Mikulla, and C. Milkereit (2021). GFZ contribution to the COSEISMIQ seismic network, *GFZ Data Services, Other/Seismic Network* doi: 10.14470/9D7564946595.

Duran, A. (2021). Numerical sensitivity kernels in elastic media for imaging purposes and seismic tomography in the Hengill geothermal field, PhD manuscript, ETH Zurich.

Elders, W., G. Friðleifsson, and A. Albertsson (2014). Drilling into magma and the implications of the Iceland Deep Drilling Project (IDDP) for high-temperature geothermal systems worldwide, *Geothermics* **49,** 111–118.

Foulger, G. R., and D. Toomey (1989). Structure and evolution of the Hengill-Grensdalur Volcanic Complex, Iceland: Geology, geophysics, and seismic tomography, *J. Geophys. Res.* **94,** no. B12, 17,511–17,522.

Franzson, H., G. Guðfinnsson, H. Helgadóttir, and J. Frolova (2010). *Porosity, Density and Chemical Composition Relationships in Altered Icelandic Hyaloclastites*, CRC Press Inc., Boca Raton, Florida.

Franzson, H., B. R. Kristjánsson, G. Gunnarsson, G. Björnsson, A. Hjartarson, B. Steingrímsson, E. Gunnlaugsson, and G. Gíslason (2005). The Hengill-Hellisheiði geothermal field. Development of a conceptual geothermal model, *Proc. World Geothermal Congress*, Antalya, Turkey, 1–7.

Friðleifsson, G., B. Pálsson, A. L. Albertsson, B. Stefánsson, E. Gunnlaugsson, J. Ketilsson, and P. Gíslason (2015). IDDP-1 drilled into magma—World's first magma-EGS system created, *World Geothermal Congress*, 19–25.

Friðleifsson, G. Ó., H. Ármannsson, K. Árnason, I. Þ. Bjarnason, and G. Gíslason (2003). Iceland Deep Drilling Project (IDDP): Drilling targets for supercritical fluid, *Int. Geothermal Conference*, Citeseer, Reykjavík, Iceland.

Gasperikova, E., G. K. Rosenkjaer, K. Arnason, G. A. Newman, and N. J. Lindsey (2015). Resistivity characterization of the Krafla and Hengill geothermal fields through 3D MT inverse modeling, *Geothermics* **57,** 246–257.

Glen, J. M., L. Liberty, E. Gasperikova, D. Siler, J. Shervais, B. Ritzinger, N. Athens, and T. Earney (2017). Geophysical investigations and structural framework of geothermal systems in west and south-central Idaho; Camas Prairie to Mountain Home, *Proc. 42nd Workshop on Geothermal Reservoir Engineering*, Stanford, California, 1021–1033.

Grigoli, F., J. Clinton, T. Diehl, P. Kaestli, L. Scarabello, T. Ágústsdóttir, S. Kristjansdottir, R. Magnusson, C. Bean, M. Broccardo, *et al.* (2022). Monitoring microseismicity in the Hengill Geothermal Field, Iceland, *Sci. Data* **9,** doi: 10.1038/s41597-022-01339-w.

Haberland, C., and O. Ritter (2016). GIPP: Geophysical Instrument Pool Potsdam, *J. Large Scale Res. Facil.* **2,** no. A64, doi: 10.17815/jlsrf-2-128.

Hanka, W., J. Saul, B. Weber, J. Becker, P. Harjadi, and , and GITEWS Seismology Group (2010). Real-time earthquake monitoring for tsunami warning in the Indian Ocean and beyond, *Nat. Hazards Earth Syst. Sci.* **10,** no. 12, 2611–2622.

Hillers, G., M. Campillo, Y. Ben-Zion, and P. Roux (2014). Seismic fault zone trapped noise, *J. Geophys. Res.* **119,** no. 7, 5786–5799.

Hjörleifsdóttir, V., S. Ó. Snæbjörnsdóttir, G. Gunnarsson, B. R. Kristjánsson, K. Vogfjord, K. Jónsdóttir, S. Hjaltadóttir, K. Ágústsson, Þ. Ágústsdóttir, M. McKenzie, *et al.* (2020). Induced earthquakes in the Hellisheiði geothermal field, Iceland, *Proc. World Geothermal Congress*, Reykjavik, Iceland.

Jolie, E., L. C. Gutiérrez-Negrín, K. Kieling, D. Liotta, C. A. Galván, G. Páll, Á. B. Hersir, P. Deb, A. A. Aguilar, I. Ö. Thorbjörnsson, *et al.* (2020). The GEMex project: Developing Los Humeros (Mexico) as a Superhot Geothermal Site, *Proc. World Geothermal Congress*, Reykjavik, Iceland.

Jousset, P., C. Haberland, K. Bauer, and K. Arnason (2011). Hengill geothermal volcanic complex (Iceland) characterized by integrated geophysical observations, *Geothermics* **40,** no. 1, 1–24.

Jousset, P., T. Reinsch, T. Ryberg, H. Blanck, A. Clarke, R. Aghayev, G. P. Hersir, J. Henninges, M. Weber, and C. M. Krawczyk (2018).

Dynamic strain determination using fibre-optic cables allows imaging of seismological and structural features, *Nat. Commun.* **9,** no. 1, doi: 10.1038/s41467-018-04860-y.

Kruszewski, M., and V. Wittig (2018). Review of failure modes in supercritical geothermal drilling projects, *Geotherm. Energy* **6,** no. 1, 1–29.

Lautze, N., D. Thomas, D. Waller, N. Frazer, N. Hinz, and G. Apuzen-Ito (2017). Play fairway analysis of geothermal resources across the state of Hawaii: 3. Use of development viability criterion to prioritize future exploration targets, *Geothermics* **70,** 406–413.

Li, K. L., C. Abril, O. Gudmundsson, and G. B. Gudmundsson (2019). Seismicity of the Hengill area, SW Iceland: Details revealed by catalog relocation and collapsing, *J. Volcanol. Geotherm. Res.* **376,** 15–26.

Lindsey, N. J., H. Rademacher, and J. B. Ajo-Franklin (2020). On the broadband instrument response of fiber-optic DAS Arrays, *J. Geophys. Res.* **125,** no. 2, e2019JB018145.

Mousavi, S. M., W. L. Ellsworth, W. Zhu, L. Y. Chuang, and G. C. Beroza (2020). Earthquake transformer—An attentive deep-learning model for simultaneous earthquake detection and phase picking, *Nat. Commun.* **11,** no. 1, 1–12.

Nooshiri, N., C. Bean, T. Dahm, F. Grigoli, S. Kristjánsdóttir, A. Obermann, and S. Wiemer (2022). A multibranch, multitarget neural network for rapid point-source inversion in a microseismic environment: Examples from the Hengill Geothermal Field, Iceland, *Geophys. J. Int.* **229,** no. 2, 999–1016.

Peterson, J. R. (1993). Observations and modeling of seismic background noise, *U.S. Geol. Surv.* doi: 10.3133/ofr93322.

Reinsch, T., P. Dobson, H. Asanuma, E. Huenges, F. Poletto, and B. Sanjuan (2017). Utilizing supercritical geothermal systems: A review of past ventures and ongoing research activities, *Geotherm. Energy* **5,** no. 1, 1–25.

Reykjavík Energy (Iceland) (2016). OR—Reykjavik Energy, International Federation of Digital Seismograph Networks, *Data Set*, doi: 10.7914/sn/or.

Rossi, C., F. Grigoli, S. Cesca, S. Heimann, P. Gasperini, V. Hjörleifsdóttir, T. Dahm, C. J. Bean, S. Wiemer, L. Scarabello, *et al.* (2020). Full-waveform based methods for microseismic monitoring operations: An application to natural and induced seismicity in the Hengill Geothermal Area, Iceland, *Adv. Geosci.* **54,** 129–136.

Roux, P., and Y. Ben-Zion (2017). Rayleigh phase velocities in Southern California from beamforming short-duration ambient noise, *Geophys. J. Int.* **211,** no. 1, 450–454.

Rybach, L. (2014). Geothermal power growth 1995–2013—A comparison with other renewables, *Energies* **7,** no. 8, 4802–4812.

Sánchez-Pastor, P., A. Obermann, T. Reinsch, T. Ágústsdóttir, G. Gunnarsson, S. Tómasdóttir, V. Hjörleifsdóttir, G. Hersir, K. Ágústsson, and S. Wiemer (2021). Imaging high-temperature geothermal reservoirs with ambient seismic noise tomography, a case study of the Hengill geothermal field, SW Iceland, *Geothermics* **96,** 102207, doi: 10.1016/j.geothermics.2021.102207.

Schimmel, M., E. Stutzmann, and S. Ventosa (2017). Measuring group velocity in seismic noise correlation studies based on phase coherence and resampling strategies, *IEEE Trans. Geosci. Remote Sens.* **55,** no. 4, 1928–1935.

Shi, P., F. Grigoli, F. Lanza, S. Wiemer, G. Beroza, and L. Scarabello (2022). MALMI: An automated earthquake detection and location workflow based on machine learning and waveform migration, *Seismol. Res. Lett.* doi: 10.1785/0220220071.

Sæmundsson, K. (1992). Geology of the Thingvallavatn area, *Oikos* **64,** 40–68.

Sæmundsson, K., M. Á. Sigurgeirsson, and G. Ó. Friðleifsson (2020). Geology and structure of the Reykjanes volcanic system, Iceland, *J. Volcanol. Geotherm. Res.* **391,** 106501, doi: 10.1016/j.jvolgeores.2018.11.022.

Spudich, P., and J. B. Fletcher (2008). Observation and prediction of dynamic ground strains, tilts, and torsions caused by the Mw6.0 2004 Parkfield, California, earthquake and aftershocks, derived from UPSAR array observations, *Bull. Seismol. Soc. Am.* **98,** no. 4, 1898–1914.

Staingrimsson, B. (1990). Evidence of a supercritical fluid at depth in the Nesjavallir field, *Proc. 15th Workshop on Geothermal Reservoir Engineering*, Stanford University, Stanford, California.

Strollo, A., D. Cambaz, J. Clinton, P. Danecek, C. P. Evangelidis, A. Marmureanu, L. Ottemöller, H. Pedersen, R. Sleeman, K. Stammler, *et al.* (2021). EIDA: The European integrated data archive and service infrastructure within ORFEUS, *Seismol. Soc. Am.* **92,** no. 3, 1788–1795.

Stupazzini, M., R. Paolucci, and H. Igel (2009). Near-fault earthquake ground-motion simulation in the Grenoble valley by a high-performance spectral element code, *Bull. Seismol. Soc. Am.* **99,** no. 1, 286–301.

Swiss Seismological Service (SED) at ETH Zurich (2018). COSEISMIQ—COntrol SEISmicity and Manage Induced earthQuakes, *ETH Zurich, Other/Seismic Network*, doi: 10.12686/sed/networks/2c.

Swiss Seismological Service (SED) at ETH Zurich (2021). Temporary deployments associated with the DEEPEN project in the Hengill region, Iceland, *ETH Zurich, Other/Seismic Network*, doi: 10.12686/sed/networks/YM.

Taylor, G., G. Hillers, and T. Vuorinen (2021). Using array-derived rotational motion to obtain local wave propagation properties from earthquakes induced by the 2018 geothermal stimulation in Finland, *Geophys. Res. Lett.* **48,** no. 6, e2020GL090403, doi: 10.1029/2020GL090403.

Tryggvason, A., S. T. Rögnvaldsson, and O. G. Flóvenz (2002). Three-dimensional imaging of the P- and S-wave velocity structure and earthquake locations beneath Southwest Iceland, *Geophys. J. Int.* **151,** no. 3, 848–866.

Waagaard, O. H., E. Rønnekleiv, A. Haukanes, F. Stabo-Eeg, D. Thingbø, S. Forbord, S. E. Aasen, and J. K. Brenne (2021). Real-time low noise distributed acoustic sensing in 171 km low loss fiber, *OSA Continuum* **4,** no. 2, 688.

Wang, K., L. Lu, V. Maupin, Z. Ding, C. Zheng, and S. Zhong (2020). Surface wave tomography of northeastern Tibetan plateau using beamforming of seismic noise at a dense array, *J. Geophys. Res.* **125,** no. 4, e2019JB018416, doi: 10.1029/2019JB018416.

Manuscript received 2 March 2022
Published online 13 July 2022